

## COMMUNICATION


 CrossMark  
 click for updates

 Cite this: *Nanoscale*, 2014, 6, 10562

 Received 30th May 2014  
 Accepted 21st July 2014

DOI: 10.1039/c4nr02980a

www.rsc.org/nanoscale

# Hot carriers in epitaxial graphene sheets with and without hydrogen intercalation: role of substrate coupling†

 Fan-Hung Liu,<sup>a</sup> Shun-Tsung Lo,<sup>\*a</sup> Chiashain Chuang,<sup>b</sup> Tak-Pong Woo,<sup>b</sup> Hsin-Yen Lee,<sup>b</sup> Chieh-Wen Liu,<sup>a</sup> Chieh-I Liu,<sup>a</sup> Lung-I Huang,<sup>bc</sup> Cheng-Hua Liu,<sup>b</sup> Yanfei Yang,<sup>c</sup> Chih-Yuan S. Chang,<sup>d</sup> Lain-Jong Li,<sup>d</sup> Patrick C. Mende,<sup>e</sup> Randall M. Feenstra,<sup>e</sup> Randolph E. Elmquist<sup>\*c</sup> and Chi-Te Liang<sup>ab</sup>

The development of graphene electronic devices produced by industry relies on efficient control of heat transfer from the graphene sheet to its environment. In nanoscale devices, heat is one of the major obstacles to the operation of such devices at high frequencies. Here we have studied the transport of hot carriers in epitaxial graphene sheets on 6H-SiC (0001) substrates with and without hydrogen intercalation by driving the device into the non-equilibrium regime. Interestingly, we have demonstrated that the energy relaxation time of the device without hydrogen intercalation is two orders of magnitude shorter than that with hydrogen intercalation, suggesting application of epitaxial graphene in high-frequency devices which require outstanding heat exchange with an outside cooling source.

## 1. Introduction

Graphene, which can approximate an ideal two-dimensional system, has extraordinary electrical,<sup>1,2</sup> optical,<sup>3,4</sup> mechanical<sup>5,6</sup> and thermal<sup>7,8</sup> properties and has been considered for numerous applications such as field-effect transistors,<sup>9</sup> ultra-sensitive gas sensors,<sup>10</sup> and electromechanical resonators.<sup>11</sup> To date, mechanical exfoliation,<sup>12</sup> chemical vapor deposition (CVD)<sup>13</sup> and epitaxial growth<sup>14</sup> are the three major fabrication methods for graphene-based electronic devices. Although mechanically-exfoliated graphene is of the best quality, the small size of its domains appears to limit practical device applications. On the other hand, CVD methods provide a way to produce large-area films but contamination from polymer residues may be inevitable when transferring the sheet onto a substrate. Epitaxial graphene, in contrast, can be of wafer size

and does not require subsequent transfer procedures, which is ideal for applications in high-frequency devices.<sup>15</sup>

Functionalized graphene,<sup>16–20</sup> functionalized substrates,<sup>21,22</sup> and quasi-free-standing graphene production methods<sup>23–28</sup> can improve the quality of graphene by reducing its coupling with the substrate and may make graphene-based field-effect circuits realizable by opening a band gap in some cases. However, the long-term prospects for most practical applications of graphene require efficient removal of the waste heat produced during operation, which is especially important when a graphene-based device works at high frequencies. Therefore, investigations of heat transfer from hot carriers in graphene are desirable.

In a semi-classical picture, an electron and phonon system can be described statistically by the Fermi–Dirac (FD) distribution and the Bose–Einstein (BE) distribution:

$$f_{\text{FD}}(\varepsilon) = \frac{1}{\exp[(\varepsilon - \mu)/k_{\text{B}}T_{\text{e}}] + 1}, \quad (1)$$

$$f_{\text{BE}}(\varepsilon) = \frac{1}{\exp[\varepsilon/k_{\text{B}}T_{\text{L}}] - 1}, \quad (2)$$

where  $\varepsilon$ ,  $\mu$ ,  $k_{\text{B}}$ ,  $T_{\text{e}}$ , and  $T_{\text{L}}$  are the single-particle electron energy, the chemical potential, the Boltzmann constant, the electron temperature, and the temperature of the phonon system, respectively. In the low current regime  $T_{\text{e}}$  and  $T_{\text{L}}$  are the same, reflecting the equilibrium between the phonons and charge carriers *via* electron–phonon scattering. As the injected current is increased, the external electric field will raise the total kinetic energy of the electron system. This in turn will raise the value of  $T_{\text{e}}$  and lead to energy transfer from the electron system to the substrate lattice. The magnitude of this energy transfer depends on the temperature difference between  $T_{\text{e}}$  and  $T_{\text{L}}$ , as is the case for contact between two heat reservoirs. In this situation  $T_{\text{e}}$  can be substantially higher than  $T_{\text{L}}$  and this non-equilibrium heating phenomenon is known as the charge heating effect.<sup>29</sup>

In this work, we have studied charge heating in epitaxial graphene sheets with and without hydrogen intercalation

<sup>a</sup>Graduate Institute of Applied Physics, National Taiwan University, Taipei 106, Taiwan. E-mail: shuntsunglo@gmail.com; randolph.elmquist@nist.gov

<sup>b</sup>Department of Physics, National Taiwan University, Taipei 106, Taiwan

<sup>c</sup>National Institute of Standards and Technology (NIST), Gaithersburg, MD 20899, USA

<sup>d</sup>Institute of Atomic and Molecular Sciences, Academia Sinica, Taipei 106, Taiwan

<sup>e</sup>Department of Physics, Carnegie Mellon University, Pittsburgh, PA, 15213, USA

† Electronic supplementary information (ESI) available. See DOI: 10.1039/c4nr02980a

(H-intercalation) in order to understand their energy relaxation properties. Without intercalation, the buffer layer sample has essentially no conductivity, and can be compared as in this study only when it is converted into a useful electronic material by saturation of the dangling bonds of the Si atoms. The electronic transport in the H-intercalated sample is then of high quality, when compared with a naturally conducting sample. Interestingly, however, our results show that the H-intercalated graphene sheet has a much longer energy relaxation time compared to that of epitaxial graphene without H-intercalation. This can be attributed to the reduced coupling of the sheet with the SiC substrate in the absence of covalent bonds, which are broken by H-intercalation.<sup>25,30,31</sup>

## 2. Experimental section

### 2.1 Preparation of the samples

A controlled sublimation method was used for graphene growth on a chemically-mechanically polished semi-insulating 6H-SiC (0001) surface. Before the growth process, standard procedures were applied to clean the SiC substrates. After the cleaning process, the 6H-SiC (0001) surface was placed face-to-face with a polished graphite disk and arranged in such a way that wide and uniform Newton rings could be observed under fluorescent light. The substrates were dehydrated and cleaned in a furnace at 725 °C for approximately 16 hours under Ar background gas at a pressure slightly higher than 100 kPa. After the substrate treatment, the temperature was increased and maintained at 1200 °C for 30 min. Then, for Sample A, the furnace was heated to 1950 °C at a ramping rate of 100 °C min<sup>-1</sup> and maintained at 1950 °C for 30 min to grow graphene having two layers. Here, the exposed Si atoms in the SiC (0001) lattice form partial covalent bonds with carbon atoms in the lower graphene layer or zero layer,<sup>31–33</sup> and only the top layer is conducting. Sample A was then patterned into Hall-bar geometry for electrical measurements by standard photolithography using reactive ion etching in O<sub>2</sub> plasma. Ti/Au contacts were then deposited by optical lithography and a lift-off process.

The substrate and growth conditions for Sample B were the same, except that the final temperature was reduced to 1600 °C and the annealing time was increased to 1 hour. These conditions result in the production of so-called zero-layer graphene which is covalently bonded to the top-most layer of Si atoms and is non-conducting. Hall bars were fabricated as described above, and the measured average sheet resistivity of the device described here was 1.08 MΩ at 23 °C. After the process of Hall-bar production, the sample was heated again in the furnace for 24 hours at 710 °C ± 10 °C under a forming gas (96% Ar + 4% H<sub>2</sub>) background at a total pressure slightly higher than 100 kPa. During this process, hydrogen atoms were intercalated into the graphene–SiC interface.<sup>25,34,35</sup> The influence of covalent bonding between carbon atoms of the bottom-layer graphene and Si atoms of the SiC substrate can be eliminated by this process, and moreover the dangling bonds at the interface are passivated by bonding with hydrogen atoms, effectively decoupling the graphene sheet from the SiC substrate. After H-intercalation, the sheet resistivity of Sample B was measured to be 22.7 kΩ at

23 °C, which was similar to that of Sample A and indicated substantial breaking of the covalent bonds.

### 2.2 Electrical measurements

Standard four-terminal electrical measurements were performed on Sample A and Sample B. The magnetic field was applied perpendicular to the plane of the graphene sheet. DC current was injected by using a constant current source (Keithley 236). The voltage probes for the measurements of resistances  $R_{xx}$  and  $R_{yy}$  are separated from the source and drain to minimize the influence of contact resistance. For two-dimensional systems like graphene, one can then obtain resistivities  $\rho_{xx}$  and  $\rho_{xy}$  by  $\rho_{xx} = R_{xx}w/l$  and  $\rho_{xy} = R_{xy}$ , where  $w$  is the width of the sample and  $l$  is the distance between the two voltage probes for  $R_{xx}$ . From the sign of Hall resistivity  $\rho_{xy}$ , the type of carriers for transport could be identified. The results show that Sample A is n-type whereas Sample B with H-intercalation is p-type. This behavior is consistent with reports in the literature demonstrating that intercalation leads to the robust p-type doping.<sup>25,30</sup> For the discussion here, only the magnitude of  $\rho_{xy}$  related to the carrier density is considered.

## 3. Results and discussion

We have noted from the AFM image in Fig. 1a for Sample A, the epitaxial graphene on SiC (0001) has surface roughness on the order of 10 nm. This reflects the step-like terrace structure that was formed due to the miscut angle of the wafer relative to the crystalline basal plane, and by the sublimation of Si from the edges of SiC atomic planes in the annealing stage of graphene growth. In Sample B, where annealing occurred at a lower temperature, there is no terrace formation and the surface is composed of atomic planes with one-half unit cell height (~0.75 nm) as observed in Fig. 1b.

Fig. 2a and d show the longitudinal resistivity  $\rho_{xx}$  as a function of magnetic field at various measurement temperatures (equivalent to the lattice temperature)  $T_1$  for Sample A and Sample B. The currents  $I_A = 5 \mu\text{A}$  and  $I_B = 7 \mu\text{A}$  were applied for these  $T$ -dependent measurements. At lower fields around zero magnetic field  $B = 0$ , weak localization dominates due to quantum interference and negative magneto-resistivity is observed in the sense that  $\rho_{xx}$  decreases with increasing magnetic field. Fig. 2b and e show the absolute value of the corresponding Hall resistivity for each sample, both of which are  $T$ -independent. From the Hall slope  $\delta\rho_{xy}/\delta B$  defined as  $\delta\rho_{xy}/\delta B \equiv B/(ne)$ , the carrier densities of  $n_{\text{H}}^{\text{A}} = 1.60 \times 10^{13} \text{ cm}^{-2}$  and  $p_{\text{H}}^{\text{B}} = 1.85 \times 10^{13} \text{ cm}^{-2}$  are estimated for Sample A and Sample B. Although the Hall mobility of Sample A ( $\approx 890 \text{ cm}^2/\text{V s}$ ) appears to be slightly higher than that for Sample B ( $\approx 770 \text{ cm}^2 \text{ V}^{-1} \text{ s}^{-1}$ ), we can show that in the field of magneto-transport, the quantum mobility, rather than the classical Hall mobility is a more important physical quantity with respect to the disorder within the graphene systems. Fig. 2c and f present the results of  $\rho_{xx}(B)$  at various driving currents  $I$  and a fixed  $T_1$ , in which a clear dependence on  $I$  is observed.<sup>36,37</sup> Hence by comparing  $\rho_{xx}(B, I)$  with  $\rho_{xx}(B, T)$ , that is, by using the resistivity

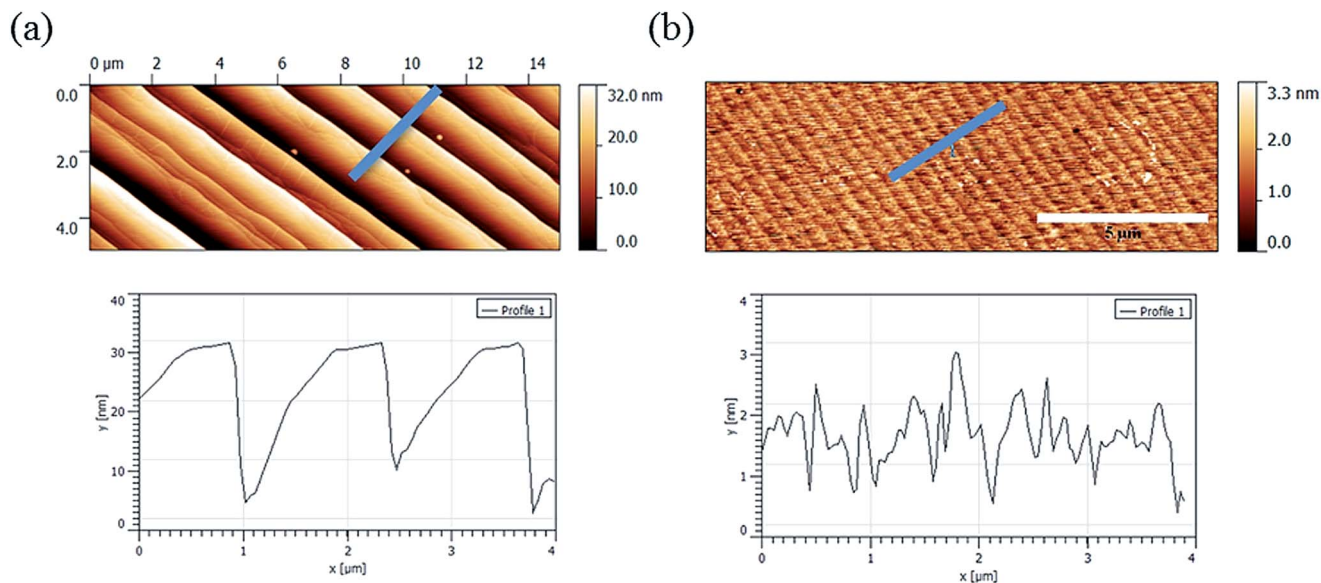


Fig. 1 AFM results including height and phase spatial images for samples (a) without and (b) with H-intercalation. The bottom panel shows the line profile along the line denoted in the height image.

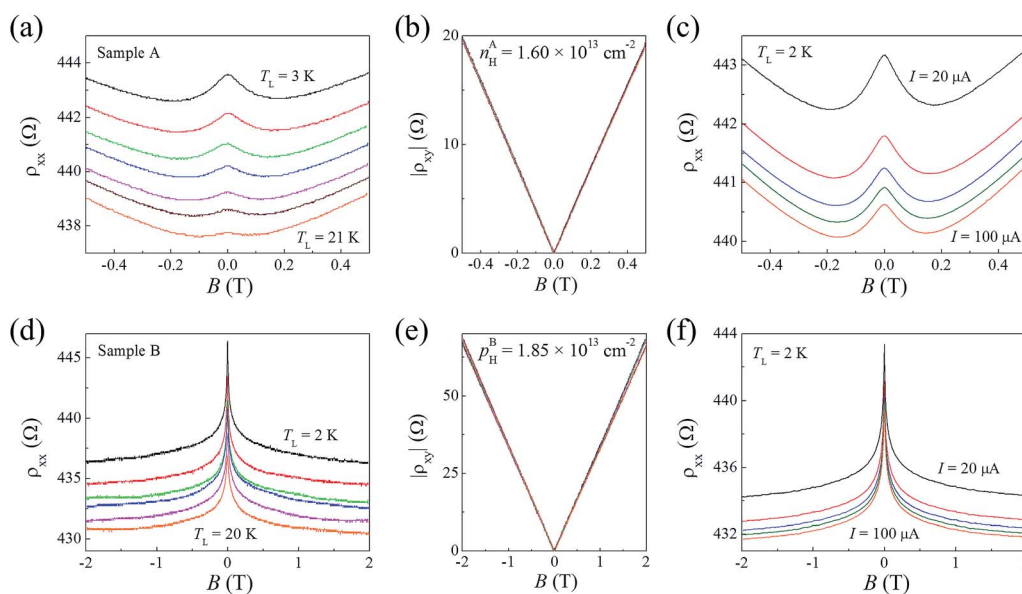


Fig. 2 (a & b) Magneto-resistivity  $\rho_{xx}(B)$  and Hall resistivity  $|\rho_{xy}(B)|$  at various temperatures  $T_L$  for Sample A. From top to bottom in (a),  $T_L = 3$  K, 5 K, 7 K, 9 K, 12 K, 15 K, and 21 K. (c)  $\rho_{xx}(B)$  at different input currents  $I$  with  $T_L$  fixed at 2 K. From top to bottom:  $I = 20$   $\mu$ A, 50  $\mu$ A, 70  $\mu$ A, 85  $\mu$ A, and 100  $\mu$ A. (d)–(f) The corresponding results for Sample B. From top to bottom in (d),  $T_L = 2$  K, 5 K, 8 K, 10 K, 15 K, and 20 K. The sequence of the input current in (f) is the same as in (c). The lattice temperature is also constantly fixed at  $T_L \approx 2$  K.

value as a self-thermometer as clearly demonstrated in samples which show insulating behavior in the literature,<sup>29,38,39</sup> we were able to determine the effective carrier temperature  $T_{cc}$ . The obtained results are presented in Fig. 3. We have noted that for the same currents,  $T_{cc}$  in Sample B is higher than that in Sample A, suggesting that it requires less work to raise the mean kinetic energy of carriers in Sample B than in Sample A.

In the seminal report of Wennberg *et al.*,<sup>29</sup> which deals with the energy transfer between charged carriers and the lattice by considering the two-bath model, it was proposed that

$$T_{cc} \propto I^\alpha, \quad (3)$$

where  $\alpha = 2/(p + 2)$  and  $p$  is the exponent for the temperature dependence of the inelastic scattering rate  $\tau_{in}^{-1} \propto T^p$ . It can be found from Fig. 3 that  $T_{cc}(I)$  of our samples follows the same trend as eqn (3) with  $p \approx 2$ , that is,  $\alpha \approx 0.5$ . This result indicates the importance of carrier-phonon scattering.<sup>40,41</sup> Given the relation  $T_{cc}(I)$ , one can further calculate the energy-loss rate  $P_{cc}$ , the average rate of energy loss per carrier, which is usually related to the carrier and lattice temperatures as

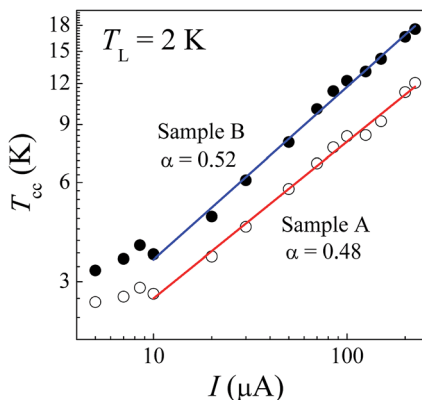


Fig. 3 Effective carrier temperature  $T_{cc}$  versus input current  $I$  on a log–log scale.

$$P_{cc} = A(T_{cc}^{\beta} - T_L^{\beta}), \quad (4)$$

where  $A$  and  $\beta$  are the parameters relevant to the scattering mechanism for energy relaxation.<sup>42</sup> In the model of Wennberg *et al.*,  $\beta = p + 2$ . Experimentally,  $P_e$  is determined as  $P_{cc} = I^2 R_{xx} / (mw)$ . Moreover, its relation with energy relaxation time  $\tau_e$  can be expressed by

$$P_{cc} = \frac{k_B(T_{cc} - T_L)}{\tau_e}. \quad (5)$$

Fig. 4a and d show that the energy-loss rate of both samples increases with  $T_{cc}$  following the power-law behavior of eqn (4). In the low- $I$  region where  $T_{cc} < 3$  K,  $P_{cc}$  deviates from the power-law dependence and thus eqn (5) cannot be used for the

determination of  $\tau_e$ . The underlying reason is that a low  $I$  cannot raise  $T_{cc}$  as presented in Fig. 3. The red lines denote the characteristic exponents which are obtained by averaging the power-law fitting results for each field. Such fits were thereby performed at current levels high enough to remove the equilibrium between carrier and phonon systems. The larger slope in Fig. 4d shows that the energy of Sample B increases faster than that of Sample A, however. For Sample B, the average exponent of  $\beta \approx 4.76$  is obtained whereas for Sample A it is  $\beta \approx 4.07$ . The obtained values are consistent with the existing results on exfoliated and CVD-grown graphene, demonstrating that  $\beta \approx 4$ .<sup>42–44</sup> In addition, the magnitude of  $P_{cc}$  is about two orders of magnitude smaller for Sample B compared to Sample A for similar temperatures. Since  $P_{cc}$  is inversely proportional to  $\tau_e$  according to eqn (5), the magnitude of  $\tau_e$  is larger for Sample B compared to Sample A as shown in Fig. 4b and e. We have also plotted  $\tau_e$  as a function of input current  $I$  in Fig. 4c and f. The power-law behavior can still be observed. Our charge heating measurements at various B show consistent results, suggesting the validity of using the resistivity value as a thermometer.

In the epitaxial graphene systems studied here the cooling of hot carriers is related to interactions with surface phonons of the SiC substrates,<sup>45</sup> giving rise to  $\beta = 4$  as described in ref. 42. At temperatures  $T_{cc}$  above the Bloch–Grüneisen temperature  $T_{BG}$ , the energy-loss rate is predicted to be enhanced due to disorder-assisted carrier-phonon scattering and the exponent of  $\beta = 3$  can instead be found.<sup>46</sup> A graphene system with the presence of charge puddles near the Dirac point can also have enhanced  $P_{cc}$  and  $\beta = 3$  (ref. 42). In our samples,  $T_{BG}^A \approx 216$  K and  $T_{BG}^B \approx 232$  K are estimated.<sup>42</sup> Since  $T_{cc}$  is well below  $T_{BG}$  and the carrier density is high for both samples, phonons of the SiC substrate would then play a dominant role in cooling hot carriers of the graphene sheet.

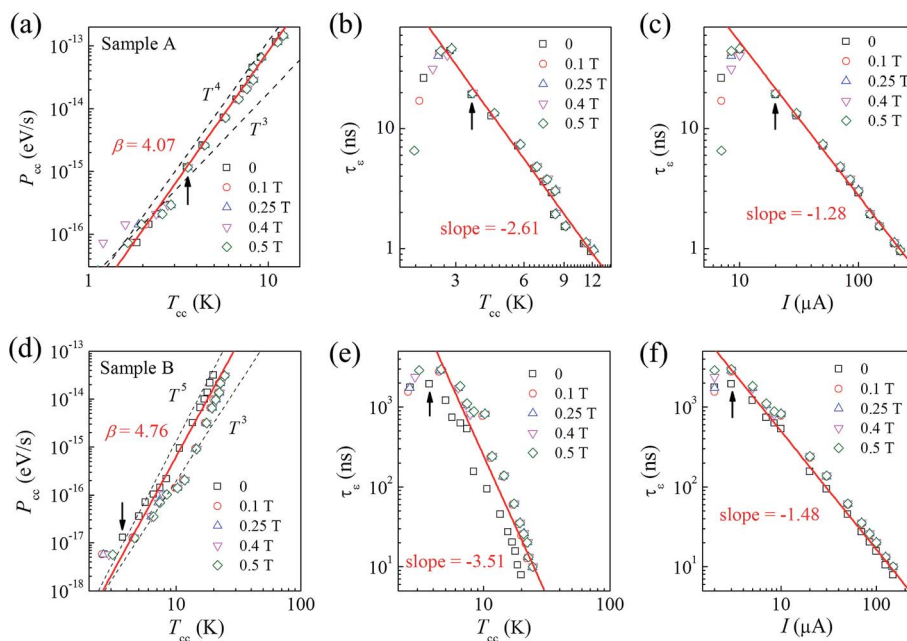


Fig. 4 (a) Carrier energy-loss rate  $P_{cc}$  versus  $T_{cc}$  at various magnetic fields on a log–log scale for Sample A. (b) Energy relaxation time  $\tau_e$  versus  $T_{cc}$  on a log–log scale. (c) Energy relaxation time  $\tau_e$  versus  $I$  on a log–log scale. (d)–(f) The corresponding results for Sample B. Arrows denote the lower bound for the fits.

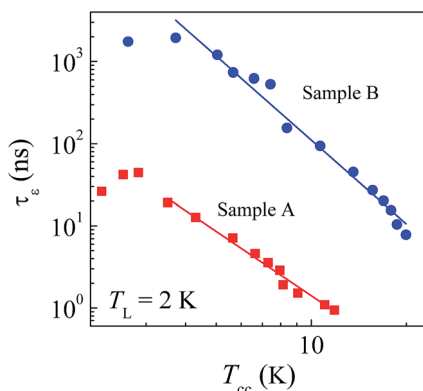


Fig. 5 Comparison of  $\tau_e(T_{cc})$  between Sample A and Sample B.

Fig. 5 compares the energy relaxation time  $\tau_e$  between the two samples. We can observe clearly that  $\tau_e$  of Sample B with H-intercalation is about two orders of magnitude longer than that of Sample A without H-intercalation. We have noted that in the work of Somphonsane *et al.*<sup>42</sup> for the same density,  $\tau_e$  for electrons is about the same as that for holes in graphene. Therefore, the observed vastly different  $\tau_e$  for electrons in Sample A compared with that for holes in Sample B cannot be ascribed to the carrier type. Instead, we infer that the coupling strength between hot electrons or holes in the graphene sheet and the phonon heat reservoir of the SiC substrate is substantially different for these two samples. A deeper examination of the characteristics of these samples aids in understanding this difference. In Fig. 6a, Sample A and Sample B have similar Raman spectra with G bands located at  $\sim 1585 \text{ cm}^{-1}$  and 2D bands at  $\sim 2680 \text{ cm}^{-1}$ , which is characteristic of graphene.<sup>20,47</sup> The absence of any significant D band contribution in the spectral region below the G band indicates that the graphene lattice is both relatively large in area and defect-free for these two samples. The 2D band is somewhat broadened for Sample A, suggesting that this sample may have some few-layer regions in addition to monolayer graphene. This observation is consistent with earlier low-energy electron microscopy (LEEM)<sup>48</sup> results for another sample produced using exactly the same annealing recipe (see Fig. S1 in the ESI†) where the presence of bilayer regions was observed over about 15% of the surface area.

However in Fig. 6b, we can observe a significant difference in the high-field magneto-transport behavior. The background resistivity for Sample A increases strongly with the magnetic field whereas it is weakly magnetic-field-dependent for Sample B. The analysis of the Shubnikov de Haas (SdH) oscillatory structure<sup>49</sup> shows that the filling factor is resolved up to about  $\nu = 94$  for Sample B but only to about  $\nu = 56$  for Sample A. These differences may reflect the relative (in)homogeneity of these samples, since the samples have similar carrier densities. As shown in Fig. S3 in the ESI,† from the slope of  $\nu$  versus  $1/B$ , which follows  $n = \nu eB/h$ , carrier densities of  $n_{\text{SdH}}^A \approx 1.60 \times 10^{13} \text{ cm}^{-2}$  and  $p_{\text{SdH}}^B \approx 1.76 \times 10^{13} \text{ cm}^{-2}$  are estimated, consistent with the values from the Hall measurements. By analyzing the amplitudes of SdH oscillations  $\Delta\rho_{xx}$  in Fig. S2 in the ESI,† we can obtain both the effective mass  $m^*$  and the quantum mobility  $\mu_q$  according to

$$\Delta\rho_{xx}(B, T) = A \exp(-\pi/(\mu_q B))D(B, T), \quad (6)$$

where  $D(B, T) = 2\pi^2 k_B m^* T / (\hbar e B) \sinh(2\pi^2 k_B m^* T / (\hbar e B))$ .<sup>50,51</sup> As shown in Fig. 6c, the fit of eqn (6) to the experimental  $\Delta\rho_{xx}(B, T)$  data for Sample B gives the effective mass of  $m_B^* \approx 0.094 m_e$ . However, the oscillations are so weak for Sample A that  $m_A^*$  is difficult to determine. We have calculated the quantum motility, which includes both large-angle and small-angle scattering events, of Sample B to be  $\mu_q^B \approx 386 \text{ cm}^2 \text{ V}^{-1} \text{ s}^{-1}$  by eqn (6) as shown in Fig. 6d.

The above observations, together with the rising background magneto-resistivity<sup>52</sup> of Sample A as shown in Fig. 6b, indicate that disorder is stronger in Sample A than in Sample B. Although our experimental findings do not give conclusive results on this point, some of this difference may be related to the greater coupling strength between the non-intercalated graphene sheet and the SiC substrate. As shown in Fig. S4,† the resistivity of the hydrogen-intercalated sample shows weak insulating behavior over the whole range of  $T$ . In contrast, the graphene sample without hydrogen intercalation shows metallic behavior in the sense that the resistivity increases with increasing  $T$ , which is characteristic of electron-phonon scattering. These results suggest that charge-phonon scattering is stronger in a sample without hydrogen intercalation compared to that in a hydrogen-intercalated device. Other factors may be

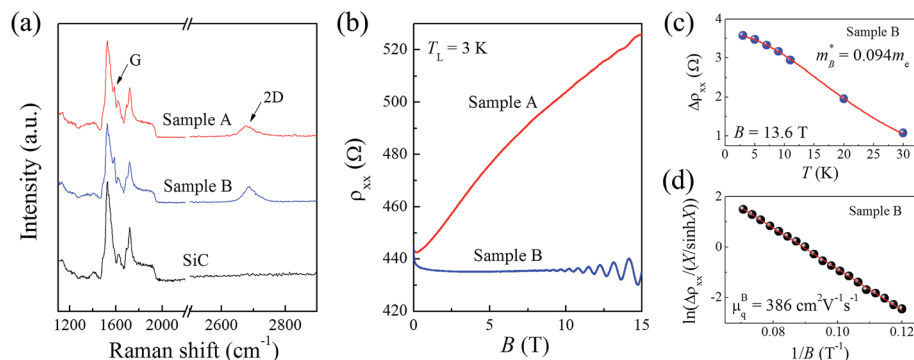


Fig. 6 (a) Raman spectrum for Sample A, Sample B, and the SiC substrate. (b)  $\rho_{xx}(B)$  for  $0 < B < 15 \text{ T}$ . (c) Amplitudes of SdH oscillations  $\Delta\rho_{xx}$  as a function of temperature  $T$  at  $B = 13.6 \text{ T}$  for Sample B. (d)  $\ln(\Delta\rho_{xx}/(X/\sinh X))$  as a function of  $1/B$  for Sample B.

the greater substrate roughness due to terrace formation and the presence of bilayer regions. Our main experimental finding has demonstrated that in the graphene sheet without H-intercalation the energy acquired from the input current is transferred to the substrate more quickly than in the sample with H-intercalation, *i.e.*, more strongly coupled carriers have better ability to undergo energy transfer with the supporting substrate than the weakly-coupled ones. With H-intercalation, the carrier-phonon coupling strength is reduced and the energy relaxation time is longer (see Fig. S5†). Such behavior is important especially when the device works at high frequencies.

## 4. Conclusions

We have investigated hot carrier effects caused by current heating on epitaxial graphene sheets with and without H-intercalation. It has been shown that intercalation of hydrogen atoms can assist in decoupling the graphene sheet and the SiC substrate, and can thus reduce scattering and increase the mobility of the device. The energy relaxation time is shorter for the sample without H-intercalation compared to that with intercalation since the coupling at the interface plays an important role in the energy transfer. Therefore, although coupling between the graphene sheet and the substrate could be detrimental to the carrier mobility, it is beneficial for the removal of heat from the sheet. Our work thereby shows that as-grown epitaxial graphene could be utilized and optimized for promising applications in hot-carrier and high-frequency devices.

## Acknowledgements

We would like to thank the Ministry of Science and Technology, Taiwan for support. This work was supported in part by the U.S. National Science Foundation, grant DMR-1205275.

## References

- 1 Y. Zhang, Y.-W. Tan, H. L. Stormer and P. Kim, *Nature*, 2005, **438**, 201–204.
- 2 K. S. Novoselov, A. K. Geim, S. V. Morozov, D. Jiang, M. I. Katsnelson, I. V. Grigorieva, S. V. Dubonos and A. A. Firsov, *Nature*, 2005, **438**, 197–200.
- 3 T. Mueller, F. Xia and P. Avouris, *Nat. Photonics*, 2010, **4**, 297–301.
- 4 M. Liu, X. Yin, E. Ulin-Avila, B. Geng, T. Zentgraf, L. Ju, F. Wang and X. Zhang, *Nature*, 2011, **474**, 64–67.
- 5 M. K. Zalalutdinov, J. T. Robinson, C. E. Junkermeier, J. C. Culbertson, T. L. Reinecke, R. Stine, P. E. Sheehan, B. H. Houston and E. S. Snow, *Nano Lett.*, 2012, **12**, 4212–4218.
- 6 C. Lee, X. Wei, J. W. Kysar and J. Hone, *Science*, 2008, **321**, 385–388.
- 7 A. A. Balandin, S. Ghosh, W. Bao, I. Calizo, D. Teweldebrhan, F. Miao and C. N. Lau, *Nano Lett.*, 2008, **8**, 902–907.
- 8 S. Ghosh, I. Calizo, D. Teweldebrhan, E. P. Pokatilov, D. L. Nika, A. A. Balandin, W. Bao, F. Miao and C. N. Lau, *Appl. Phys. Lett.*, 2008, **92**, 151911.
- 9 F. Xia, D. B. Farmer, Y.-m. Lin and P. Avouris, *Nano Lett.*, 2010, **10**, 715–718.
- 10 F. Schedin, A. K. Geim, S. V. Morozov, E. W. Hill, P. Blake, M. I. Katsnelson and K. S. Novoselov, *Nat. Mater.*, 2007, **6**, 652–655.
- 11 J. S. Bunch, A. M. van der Zande, S. S. Verbridge, I. W. Frank, D. M. Tanenbaum, J. M. Parpia, H. G. Craighead and P. L. McEuen, *Science*, 2007, **315**, 490–493.
- 12 K. S. Novoselov, A. K. Geim, S. V. Morozov, D. Jiang, Y. Zhang, S. V. Dubonos, I. V. Grigorieva and A. A. Firsov, *Science*, 2004, **306**, 666–669.
- 13 A. N. Obraztsov, *Nat. Nanotechnol.*, 2009, **4**, 212–213.
- 14 C. Berger, Z. Song, X. Li, X. Wu, N. Brown, C. Naud, D. Mayou, T. Li, J. Hass, A. N. Marchenkov, E. H. Conrad, P. N. First and W. A. de Heer, *Science*, 2006, **312**, 1191–1196.
- 15 Y.-M. Lin, C. Dimitrakopoulos, K. A. Jenkins, D. B. Farmer, H.-Y. Chiu, A. Grill and P. Avouris, *Science*, 2010, **327**, 662.
- 16 G. Eda, Y.-Y. Lin, C. Mattevi, H. Yamaguchi, H.-A. Chen, I. S. Chen, C.-W. Chen and M. Chhowalla, *Adv. Mater.*, 2010, **22**, 505–509.
- 17 S. H. Cheng, K. Zou, F. Okino, H. R. Gutierrez, A. Gupta, N. Shen, P. C. Eklund, J. O. Sofo and J. Zhu, *Phys. Rev. B: Condens. Matter Mater. Phys.*, 2010, **81**, 205435.
- 18 Q. Tang, Z. Zhou and Z. Chen, *Nanoscale*, 2013, **5**, 4541–4583.
- 19 S.-T. Lo, C. Chuang, R. K. Puddy, T. M. Chen, C. G. Smith and C. T. Liang, *Nanotechnology*, 2013, **24**, 165201.
- 20 Y.-F. Lu, S.-T. Lo, J.-C. Lin, W. Zhang, J.-Y. Lu, F.-H. Liu, C.-M. Tseng, Y.-H. Lee, C.-T. Liang and L.-J. Li, *ACS Nano*, 2013, **7**, 6522–6532.
- 21 C. R. Dean, A. F. Young, I. Meric, C. Lee, L. Wang, S. Sorgenfrei, K. Watanabe, T. Taniguchi, P. Kim, K. L. Shepard and J. Hone, *Nat. Nanotechnol.*, 2010, **5**, 722–726.
- 22 S.-Y. Chen, P.-H. Ho, R.-J. Shiue, C.-W. Chen and W.-H. Wang, *Nano Lett.*, 2012, **12**, 964–969.
- 23 K. V. Emtsev, A. Bostwick, K. Horn, J. Jobst, G. L. Kellogg, L. Ley, J. L. McChesney, T. Ohta, S. A. Reshanov, J. Rohrl, E. Rotenberg, A. K. Schmid, D. Waldmann, H. B. Weber and T. Seyller, *Nat. Mater.*, 2009, **8**, 203–207.
- 24 X. Du, I. Skachko, A. Barker and E. Y. Andrei, *Nat. Nanotechnol.*, 2008, **3**, 491–495.
- 25 C. Riedl, C. Coletti, T. Iwasaki, A. A. Zakharov and U. Starke, *Phys. Rev. Lett.*, 2009, **103**, 246804.
- 26 E. Pallecchi, F. Lafont, V. Cavaliere, F. Schopfer, D. Mailly, W. Poirier and A. Ouerghi, *Sci. Rep.*, 2014, **4**, 4558.
- 27 T. Ohta, A. Bostwick, T. Seyller, K. Horn and E. Rotenberg, *Science*, 2006, **313**, 951–954.
- 28 A. Bostwick, F. Speck, T. Seyller, K. Horn, M. Polini, R. Asgari, A. H. MacDonald and E. Rotenberg, *Science*, 2010, **328**, 999–1002.
- 29 A. K. M. Wennberg, S. N. Ytterboe, C. M. Gould, H. M. Bozler, J. Klem and H. Morkoç, *Phys. Rev. B: Condens. Matter Mater. Phys.*, 1986, **34**, 4409–4411.
- 30 J. Ristein, S. Mammadov and T. Seyller, *Phys. Rev. Lett.*, 2012, **108**, 246104.
- 31 S. Forti, K. V. Emtsev, C. Coletti, A. A. Zakharov, C. Riedl and U. Starke, *Phys. Rev. B: Condens. Matter Mater. Phys.*, 2011, **84**, 125449.

- 32 S. Forti and U. Starke, *J. Phys. D: Appl. Phys.*, 2014, **47**, 094013.
- 33 S. Goler, C. Coletti, V. Piazza, P. Pingue, F. Colangelo, V. Pellegrini, K. V. Emtsev, S. Forti, U. Starke, F. Beltram and S. Heun, *Carbon*, 2013, **51**, 249–254.
- 34 J. A. Robinson, M. Hollander, M. LaBella, K. A. Trumbull, R. Cavaleiro and D. W. Snyder, *Nano Lett.*, 2011, **11**, 3875–3880.
- 35 S. Hertel, D. Waldmann, J. Jobst, A. Albert, M. Albrecht, S. Reshanov, A. Schöner, M. Krieger and H. B. Weber, *Nat. Commun.*, 2012, **3**, 957.
- 36 X. P. A. Gao, G. S. Boebinger, A. P. Mills, A. P. Ramirez, L. N. Pfeiffer and K. W. West, *Phys. Rev. Lett.*, 2005, **94**, 086402.
- 37 I. V. Soldatov, A. V. Germanenko, G. M. Minkov, O. E. Rut and A. A. Sherstobitov, *Phys. Rev. B: Condens. Matter Mater. Phys.*, 2011, **83**, 085307.
- 38 E. Chow, H. P. Wei, S. M. Girvin, W. Jan and J. E. Cunningham, *Phys. Rev. B: Condens. Matter Mater. Phys.*, 1997, **56**, R1676–R1679.
- 39 R. Fletcher, Y. Feng, C. T. Foxon and J. J. Harris, *Phys. Rev. B: Condens. Matter Mater. Phys.*, 2000, **61**, 2028–2033.
- 40 H. P. Wei, L. W. Engel and D. C. Tsui, *Phys. Rev. B: Condens. Matter Mater. Phys.*, 1994, **50**, 14609–14612.
- 41 T. Brandes, L. Schweitzer and B. Kramer, *Phys. Rev. Lett.*, 1994, **72**, 3582–3585.
- 42 R. Somphonsane, H. Ramamoorthy, G. Bohra, G. He, D. K. Ferry, Y. Ochiai, N. Aoki and J. P. Bird, *Nano Lett.*, 2013, **13**, 4305–4310.
- 43 A. M. R. Baker, J. A. Alexander-Webber, T. Altbauer, S. D. McMullan, T. J. B. M. Janssen, A. Tzalenchuk, S. Lara-Avila, S. Kubatkin, R. Yakimova, C. T. Lin, L. J. Li and R. J. Nicholas, *Phys. Rev. B: Condens. Matter Mater. Phys.*, 2013, **87**, 045414.
- 44 S. S. Kubakaddi, *Phys. Rev. B: Condens. Matter Mater. Phys.*, 2009, **79**, 075417.
- 45 A. M. DaSilva, K. Zou, J. K. Jain and J. Zhu, *Phys. Rev. Lett.*, 2010, **104**, 236601.
- 46 J. C. W. Song, M. Y. Reizer and L. S. Levitov, *Phys. Rev. Lett.*, 2012, **109**, 106602.
- 47 A. C. Ferrari, J. C. Meyer, V. Scardaci, C. Casiraghi, M. Lazzeri, F. Mauri, S. Piscanec, D. Jiang, K. S. Novoselov, S. Roth and A. K. Geim, *Phys. Rev. Lett.*, 2006, **97**, 187401.
- 48 R. M. Feenstra and M. Widom, *Ultramicroscopy*, 2013, **130**, 101–108.
- 49 E. Tiras, S. Ardali, T. Tiras, E. Arslan, S. Cakmakyapan, O. Kazar, J. Hassan, E. Janzén and E. Ozbay, *J. Appl. Phys.*, 2013, **113**, 043708.
- 50 P. T. Coleridge, R. Stoner and R. Fletcher, *Phys. Rev. B: Condens. Matter Mater. Phys.*, 1989, **39**, 1120–1124.
- 51 S.-T. Lo, K. Y. Chen, T. L. Lin, L.-H. Lin, D.-S. Luo, Y. Ochiai, N. Aoki, Y.-T. Wang, Z. F. Peng, Y. Lin, J. C. Chen, S.-D. Lin, C. F. Huang and C. T. Liang, *Solid State Commun.*, 2010, **150**, 1902–1905.
- 52 B. Jouault, B. Jabakhanji, N. Camara, W. Desrat, C. Consejo and J. Camassel, *Phys. Rev. B: Condens. Matter Mater. Phys.*, 2011, **83**, 195417.